2020

Site-specific irrigation management in a sub-humid climate using a spatial evapotranspiration model with satellite and airborne imagery

Sandeep Bhatti
University of Nebraska-Lincoln, sandeep.bhatti@huskers.unl.edu

Derek M. Heeren
University of Nebraska-Lincoln, derek.heeren@unl.edu

J. Burdette Barker
University of Nebraska–Lincoln, burdette.barker@huskers.unl.edu

Christopher M. U. Neale
University of Nebraska-Lincoln, cneale@nebraska.edu

Wayne Woldt
University of Nebraska - Lincoln, wwoldt1@unl.edu

Site-specific irrigation management in a sub-humid climate using a spatial evapotranspiration model with satellite and airborne imagery

Sandeep Bhatti,[1] Derek M. Heeren,[1] J. Burdette Barker,[1,4] Christopher M.U. Neale,[2] Wayne E. Woldt,[1] Mitchell S. Maguire,[1] & Daran R. Rudnick[3]

1 Department of Biological Systems Engineering, University of Nebraska–Lincoln, 3605 Fair St., Lincoln, NE 68583
2 Daugherty Water for Food Global Institute at the University of Nebraska, 2021 Transformation Drive, Suite 3220, Lincoln, NE 68508
3 West Central Research and Extension Center, University of Nebraska–Lincoln, 402 W. State Farm Rd., North Platte, NE 69101
4 Natural Resources Consulting Engineers, 131 E. Lincoln Ave., Fort Collins, CO 80524

Corresponding author — D.M. Heeren, email: derek.heeren@unl.edu

Abstract

Variable Rate Irrigation (VRI) considers spatial variability in soil and plant characteristics to optimize irrigation management in agricultural fields. The advent of unmanned aircraft systems (UAS) creates an opportunity to utilize high-resolution (spatial and temporal) imagery into irrigation management due to decreasing costs, ease of operation, and reduction of regulatory constraints. This research aimed to evaluate the use of UAS data for VRI, and to quantify the potential of VRI in terms of relative crop and water response. Irrigation treatments were: (1) VRI using Landsat imagery (VRI-L), (2) VRI using UAS imagery (VRI-U), (3) uniform (U), and (4) rainfed (R). An updated remote-sensing-based evapotranspiration and water balance

Published in *Agricultural Water Management* 230 (2020) 105950

doi 10.1016/j.agwat.2019.105950
Submitted 24 May 2019; revised 22 November 2019; accepted 30 November 2019.

model, incorporating soil water measurements, was used to make prescriptions for the VRI treatments at a field site in eastern Nebraska. In 2017, the mean prescribed seasonal irrigation depth (I_p) for VRI-L was significantly greater (α=0.05) than the I_p for U for soybean. In 2018, I_p for soybean was greatest for VRI-U treatment followed by the U and VRI-L treatments, with all being significantly different from each other. No significant differences in I_p for maize were observed in 2017 or 2018. In all crop-year combinations, the VRI and U treatments had significantly greater evapotranspiration (*ET)* than the R treatment. Yield differences among treatments were not significant (except for rainfed maize compared to VRI-L in 2017). For maize in 2017, *IWUE* for VRI-L was comparable to the U treatment. The UAS imagery was a better match for the scale of crop management than Landsat imagery, particularly for thermal data. The multispectral UAS data was successfully used in the crop coefficient *ET* model for real-time irrigation, but using UAS to determine accurate canopy temperatures for surface energy balance modeling remains a challenge.

Keywords: Variable rate irrigation, Evapotranspiration, Unmanned aircraft systems, Remote sensing, Spatial variability, Soil water content

1. Introduction

Irrigated agriculture constitutes the largest freshwater usage in United States using approximately 80% of freshwater (Schaible and Aillery, 2015). Agricultural production is becoming more intensified and more yield can be obtained per unit of land and per unit of water than in the past. Over the years, new efficient irrigation systems have been introduced to increase water productivity (yield produced per unit of water diverted for irrigation) and farm profitability. Center pivot sprinkler irrigation systems are one of the most efficient irrigation systems (O'Shaughnessy et al., 2016). Center pivots are also widely adopted, constituting about 80% of total irrigated acreage in Nebraska (Johnson et al., 2011).

Conventionally, irrigation is applied uniformly intending to apply an equal depth of water to all parts of a field. Uniform irrigation is often managed according to a soil in the field having low available water capacity (*AWC*) (Daccache et al., 2015). Consequently, uniform irrigation may lead to various water losses, which may be in the form of runoff and deep percolation (*DP*). Production of high yields throughout a field with significant spatial variability in field characteristics may be difficult to achieve with uniform irrigation. Such variability may exist in terms of soil types, topography, pest attacks, crop growth, and nutrient availability (O'Shaughnessy et al., 2016). To account for

spatial variability in crop water needs, variable rate irrigation (VRI) can be implemented to manage irrigation with spatial control and precision (O'Shaughnessy et al., 2019). VRI systems can apply different amounts of irrigation to different parts of a field during a single irrigation prescription (Hedley and Yule, 2009; Evans et al., 2013; Stone and Sadler, 2016). This ability could be used to match irrigation prescriptions with spatially varying crop water needs. Spatial management capabilities of VRI systems range from relatively simple speed control systems to more complex zone control VRI systems, which can control individual or banks of sprinklers along the pivot (Evans et al., 2013; O'Shaughnessy et al., 2019).

VRI management may consider variability in multiple field characteristics to generate irrigation prescriptions. VRI can account for both spatial and temporal variation in crop water needs. Spatial variation in *AWC* in fields having significant variability in soils can be used to inform VRI and reduce water withdrawals. Lo et al. (2016) predicted that mining undepleted soil water from areas of large *AWC* in fields having significant soil variability can reduce pumpage for irrigation in Nebraska. Spatial patterns in AWC can be characterized with electrical conductivity (Hedley and Yule, 2009; Evans et al., 2013; Vanella et al., 2019) or other hydrogeophysical datasets (Finkenbiner et al., 2018). Differences in *AWC* of a field could be used to compute VRI prescriptions, which may result in reductions in energy usage and water withdrawals (Miller et al., 2017).

Spatial variability in irrigation requirements may be caused by more than just soil variability. Crop evapotranspiration (ET_c) is an important component of the soil water balance. Spatial ET_c estimates can improve the accuracy of computed spatial irrigation requirements. Studies have utilized models based on remote sensing inputs from satellite to compute spatial ET_c (Barker et al., 2018a; Stone et al., 2015; Vanella et al., 2019). Models based on energy balance equation use remote sensing inputs to estimate *ET* over large areas (Neale et al., 2012). Soil Energy Balance for Land (SEBAL; Bastiaanssen et al., 1998) and the Mapping EvapoTranspiration at high Resolution with Internalized Calibration (METRIC; Allen et al., 2007) are single-source energy models which solve for energy balance using hot (dry) and cold (wet) pixels. Real-time estimation and forecasting of spatial ET_c helps in computing real-time dynamic VRI prescription maps (Barker et al., 2018b). Barker et al. (2018b, 2019) used a spatial *ET* model called

Spatial EvapoTranspiration Modeling Interface (SETMI; Geli and Neale, 2012; Neale et al., 2012) and Landsat data to manage VRI on fields in Nebraska. The model included a water balance model based on reflectance-based crop coefficients (Neale et al., 1989) and the two-source energy balance model (TSEB; Norman et al., 1995). The TSEB model estimates components of energy balance separately for soil and plant units. The reflectance- based crop coefficient model used vegetation indices to compute spatial alfalfa-based crop coefficients (K_{cr}) and spatial ET_c.

Improvements in software capabilities, center pivot VRI systems, communication advancements, and better sensing instruments have enabled irrigation to be managed with more control and flexibility. O'Shaughnessy et al. (2016) discussed the potential of supervisory control and data acquisition systems for VRI management. Precise models are helpful to estimate water balance components and manage VRI efficiently and precisely. Presently, farmers have a variety of data sets available that could be used for making irrigation decisions. This could be challenging given the large size and complexity of data sets when collectively using them for effective irrigation management. Ongoing research is investigating the potential of fuzzy logic in decision support systems for VRI (Mendes et al., 2019). Unmanned aircraft systems (UAS) present an opportunity to collect crop canopy data at a finer temporal and spatial scale than satellite data (Woldt et al., 2018). The UAS have become more available due to decreasing costs, ease of operation, and reduction of regulatory constraints, yet research has not yet utilized UAS for real-time VRI management, particularly with an *ET*-based model.

A number of field studies on VRI have been conducted to quantify the benefits of VRI (Stone et al., 2015; Stone and Sadler, 2016; Barker et al., 2018b; Sui and Yan, 2017). Significant crop yield increases or reduction in water withdrawals resulting from VRI adoption were not observed in most studies. However, Sui and Yan (2017) found reduction in water withdrawals with VRI compared to a uniform irrigation method. Most of these studies, except for Barker et al. (2018b), have been conducted at smaller scales, which may or may not be representative of commercial-field-scale agricultural production. VRI may be an expensive investment for a producer (zone control VRI in particular) and management of a complex VRI system requires a significant

time commitment. Research is needed to document the benefits of VRI at commercial farm scales and to study the economic viability of investing in VRI systems.

The overall objective of this study was to assess the use of UAS data with an *ET* model for VRI management, and to quantify potential benefits, in terms of yield increases and reduction in water withdrawals, of VRI management as compared to the U and R treatments in a commercial producer sized field. SETMI was implemented in the study using remote sensing inputs from satellite and UAS. This study also utilized differences in *AWC* among management zones to manage irrigation treatments. Crop yield, prescribed gross irrigation depth, actual evapotranspiration (ET_a), and various irrigation efficiencies were compared among the treatments. The specific objectives of the study included: (1) quantifying and comparing crop yield and irrigation usage for different irrigation treatments, (2) improving SETMI as a decision support system using remote sensing inputs from UAS and satellite, and (3) estimating and comparing water balance response variables for different treatments.

2. Material and methods

2.1. Study site

A field site equipped with a center pivot irrigation system was used to conduct the experiment in 2017 and 2018. The field site was near Mead, Nebraska (41.165 °N, 96.430 °W) and is property of the University of Nebraska's Eastern Nebraska Research and Extension Center (ENREC). The field was irrigated with a Lindsay Corporation (Omaha, Nebraska) Zimmatic 8500 center pivot with Lindsay's Precision VRI system allowing individual sprinkler control. The field size was nearly 53 ha. Further details about the field can be found in Miller et al. (2017) and Barker et al. (2018b).

The north and south halves of the field were planted with maize and soybean, respectively, in 2017 and rotated for each half in 2018. The VRI-equipped center pivot was installed in 2014. The center pivot consisted of seven spans having a total lateral length of about 380m with sprinklers fixed on top of the lateral pipe. Soils in the field were

Study Site

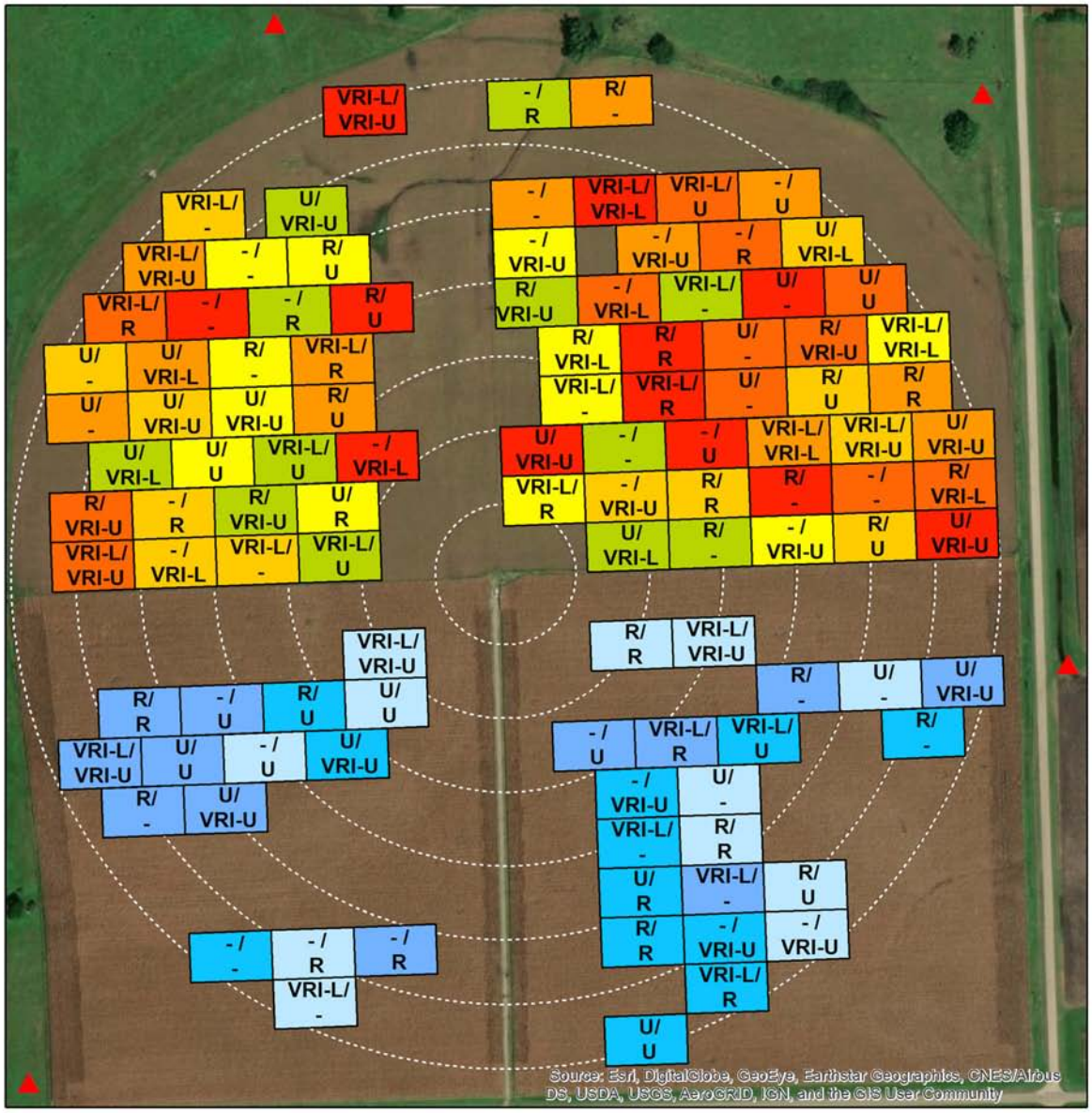

Legend

Soil Groups

North	South
1	1
2	2
3	3
4	Rain Gauges
5	
6	

0 75 150 300 m

N

Fig. 1. Plot layout of experiment in 2017 and 2018. Letters inside plots denote treatments applied in 2017/2018. '–' in plot labels is used to indicate that the plot was not used in the analysis for that year. Dotted white lines represent pivot tracks. Background basemap: World imagery from ESRI ArcMAP (Accessed on 21 November, 2018). Range of AWC values for soil blocks 1, 2, 3, 4, 5 and 6 (shown in legend) in north half is 0.20-0.23, 0.23-0.24, 0.24-0.25, 0.25-0.25, 0.26-0.27 and 0.27-0.30 m^3m^{-3}, respectively. Range of AWC values for soil blocks 1, 2, and 3 (shown in legend) in south half is 0.21-0.24, 0.25-0.26 and 0.26-0.28 m^3m^{-3}, respectively.

classified as silty clay loam and silt loam (Soil Survey Staff, 2018). Crops were planted in straight rows running roughly east-to-west. The tillage practice was no till and the field was covered with residue from previous seasons. A single crop was planted in each half every year. Uniform anhydrous ammonia injection applications were applied to half of the field in the autumn preceding maize planting for the next year.

2.2. Experimental design

The experimental design was similar to Barker et al. (2018b). The maize and soybean crops were managed as two different fields. Plots were designed along crop rows. The design of the study plots was a generalized randomized complete block design (RCBD). The design included 108 plots: 72 plots in the north and 36 plots in the south (Fig. 1). The plots were rectangular with length of ~61m and width of ~37 m. Blocking was based on the range of *AWC* in each soil class. *AWC* of each plot was computed from estimated values of field capacity (*FC*) and wilting point *(WP*) for each plot. Plots were grouped into six blocks for the north half and three blocks for the south half of the field. The number of blocks was dependent on the range of *AWC* values in each block. Each final soil block had a similar range of *AWC* of soils. The maximum variability in *AWC* values for a 1.2-m soil profile in each block was less than 40 mm. Treatments were randomly assigned to plots in each soil block and were randomized both years.

There were three treatments in 2017: variable rate irrigation using SETMI and Landsat (VRI-L), U (based on neutron probe), and R; these were applied to plots in both the north and south halves of the field. Out of 108 plots in the field, 81 plots were used for the study in 2017.

This is because one of the original intended treatments was omitted after the experiment began; these plots were excluded from the analysis for 2017. The 81 plots were equally divided among the three treatments to form a balanced design for both the north and south halves of the field.

In 2018, a new treatment, VRI using SETMI and UAS imagery (VRI-U), was added to the study. In 2018, the north half had four treatments, VRI-L, VRI-U, U, and R. The south half had three treatments, excluding the VRI-L treatment. Only 54 plots in north half and 24 plots in south half were used in the 2018 analysis because some plots were used for testing a new proprietary treatment (data not shown). The design was balanced for south and unbalanced for north. In the north, more plots in each block were attributed to the new treatment (VRI-U) to gain more knowledge on this treatment.

Irrigation was managed according to computed plot-specific water balances for the plots in the VRI treatments. For the U treatment, a single plot was chosen in each half of the field. These plots had *AWC* near the lower 10th percentile of *AWC* for plots under the U treatment in the respective half of the field. R plots were not irrigated throughout the season.

2.3. Acquired data

2.3.1. Weather data

Weather data was acquired from the High Plains Regional Climate Center's (HPRCC) Automated Weather Data Network. Data from the Memphis 5 N (41.15 °N, 96.417 °W; HPRCC) weather station was used (Shulski et al., 2018). This station was at a distance of approximately 1 km southeast of research field. Reference evapotranspiration (ET_r) was computed from the hourly and daily weather data from the station using the ASCE Standardized Tall Reference Evapotranspiration equation (ASCE-EWRI, 2005). ET_r was computed on hourly time step throughout the 24 -h period and summed up to a daily time step. Negative values of ET_r during the night hours were also considered when the hourly values from a given day were added to compute daily ET_r.

For irrigation scheduling, daily ET_r and growing degree days (*GDD*) were forecasted for the remainder of the season after the most recent

data. Daily average values of maximum and minimum air temperature (for *GDD*s) and ET_r were computed from 20 years of historic weather data. Historic data from years 1997–2016 and 1998–2017 were used in 2017 and 2018, respectively. This data was obtained from the same weather station. These forecasted values along with forecasted K_{cr} values were then used to predict ET_c. The method used for forecasting K_{cr} is discussed below in section 2.4.2. Finally, irrigation needs were computed using forecasted ET_c values. Forecasted precipitation was not taken into account when irrigation prescriptions were designed, consistent with Barker et al. (2018b).

Four tipping bucket type rain gauges were installed in different locations around the field. The rain gauges were ISCO Model 764 (Teledyne ISCO, Lincoln, Nebraska) in 2017 and TR-525 USW (Texas Electronics, Dallas, Texas) in 2018. Multiple rain gauges were used to accurately capture mean rainfall received by the field. Rain gauges were calibrated before installation. Correction values calculated in the calibration process were applied to the data. The arithmetic mean of all four rain gauges was used to represent rainfall for a given day. Data were excluded from the arithmetic mean during periods when a rain gauge was malfunctioning. Rainfall data was recorded on an event basis using HOBO dataloggers (Onset, Bourne, Massachusetts) and the sum of events was used to represent rainfall on a daily basis. In 2018, rainfall data from the weather station was used until 11 May due to erroneous measurements resulting from improper installation of field rain gauges. Rain gauge data from the field was used for remainder of the season.

Historic (1981–2010) average rainfall from May to October was about 540mm near the research field (NCEI, n.d.-a). This data was recorded by the National Weather Service Global Historical Climate Network's weather station Mead 6S which was situated about 6.5 km southwest of the field. The cumulative rainfall for months May to October recorded by the rain gauges at the field was 643 and 691mm in 2017 and 2018, respectively. These two years could be considered wetter than normal years.

Atmospheric pressure was obtained from Neb Field 3 Cosmic-ray Soil Moisture Observing System (COSMOS) station (Zreda, n.d.). Pressure data was used as an input into the TSEB model.

2.3.2. Remote sensing data

Remote sensing inputs from both satellite and UAS were used in the model. **Table 1** lists the Landsat and UAS imagery used in the model, respectively. In 2017, few Landsat 7 images were usable for the field. Only one Landsat 7 imagery each for the north and south halves of the field was considered good. In 2018, no usable Landsat image was acquired for the second half of the growing season. A total of 14 UAS image mosaics were used in 2018 for the VRI-U treatment.

Satellite imagery from Landsat 7 Enhanced Thematic Mapper Plus (ETM+), Landsat 8 Operational Land Imager (OLI) and Landsat 8 Thermal Infrared Sensor (TIRS) were used in the model. The Level-1 raw and Level-2 surface reflectance imagery were retrieved from U.S. Geological Survey. The thermal infrared bands from Level-1 imagery

Table 1. List of dates of satellite and UAS imagery used in VRI treatments in 2017 and 2018.

Image Dates in 2017			*Image Dates in 2018*		
Source	*Date*	*TSEB*	*Source*	*Date*	*TSEB*
Maize 2017			***Soybean 2018***		
Landsat 8	May 13, 2017	No	Landsat 7	May 8, 2018	No
Landsat 8	May 29, 2017	No	Landsat	8 May 16, 2018	No
Landsat 7	June 6, 2017	No	Landsat	7 May 24, 2018	No
Landsat 8	June 14, 2017	Yes	Landsat	8 June 1, 2018	No
Landsat 8	June 30, 2017	Yes	Landsat	8 July 3, 2018	Yes
Landsat 8	July 16, 2017	Yes	Landsat	7 July 11, 2018	No
Landsat 8	August 17, 2017	Yes	Landsat	8 July 19, 2018	Yes
Landsat 8	September 2, 2017	Yes			
Soybean 2017			***Maize and Soybean 2018***		
Landsat 8	May 29, 2017	No	UAS	May 10, 2018	No
Landsat 8	June 14, 2017	No	UAS	May 30, 2018	No
Landsat 8	June 30, 2017	Yes	UAS	June 5, 2018	No
Landsat 8	July 16, 2017	Yes	UAS	June 18, 2018	No
Landsat 8	August 17, 2017	Yes	UAS	June 27, 2018	No
Landsat 7	August 25, 2017	No	UAS	July 2, 2018	No
Landsat 8	September 2, 2017	Yes	UAS	July 6, 2018	No
Landsat 8	October 20, 2017	No	UAS	July 11, 2018	No
			UAS	July 24, 2018	No
			UAS	August 1, 2018	No
			UAS	August 9, 2018	No
			UAS	August 29, 2018	No
			UAS	September 17, 2018	No
			UAS	September 26, 2018	No

were used in TSEB model and multispectral bands from Level-2 imagery were used for computing vegetation index SAVI. Since a new Landsat 8 image is collected after every 16 days, Landsat 7 imagery was used to increase the frequency of useful images potentially to every eight days. However, Landsat 7 imagery is subject to missing data because of a scan line correction problem (USGS, 2018). If such were the case, the image would not be used for the half of the field that was affected. Images with cloud cover above the field or close were not used in the study. Thermal infrared imagery acquired from a satellite could be calibrated using high-resolution thermal infrared imagery captured from UAS (Ramirez-Cuesta et al., 2017). This calibration method utilizes the comparison of UAS imagery acquired on the satellite overpass days with corresponding satellite imagery. Since there was only one UAS imagery taken on a satellite overpass day in 2018 (July 11), thermal infrared imagery from Landsat was calibrated using an atmospheric correction method. Atmospheric corrections for thermal infrared images were based on parameters calculated using the Atmospheric Correction Parameter Calculator web application (Barsi et al., 2003) and included emissivity calculations similar to Brunsell and Gilles (2002) as in Barker et al. (2018a,b). Ground-based weather data were used for obtaining parameters for atmospheric corrections. Thermal infrared images with low atmospheric transmission values (< 0.6) as calculated by the web application were not used. Thermal infrared corrections were applied using ERDAS Imagine 2014 (Hexagon Geospatial, Madison, AL) software in 2017 and ArcGIS 10.4 (ESRI, Redlands, CA) in 2018.

In 2018, multispectral imagery from UASs was collected using a MicaSense (Seattle, Washington) RedEdge multispectral sensor. The UAS imagery was captured approximately once a week with the exception of fewer imagery towards end of the season due to logistical reasons. The imagery was captured at a ground resolution of approximately 17 cm, and then was processed and calibrated using Pix4D (San Francisco, California) software. It was reprocessed to a resolution of 1m and georeferenced using ArcGIS (Esri, Redlands, California) software to input into SETMI. Ortho imagery (60 cm resolution) acquired from the National Agriculture Imagery Program (NAIP) was used for georeferencing and root mean square error (RMSE) of 1.5m on an average was obtained during this process.

2.3.3. Soil water content data

Soil volumetric water content (θ) was monitored using two neutron probes (NP), model 503 Elite Hydroprobe (CPN, Concord, California), referred to as probes E1 and E2. Aluminum NP access tubes, having a diameter of 5.1 cm, were used to monitor θ at different depths. The depths of measurement were 15, 30, 46, 76, 107, 137 and 168 cm. Tubes were installed near the geometric center of each plot. Tubes were installed between two plants with an offset distance of 0.2-0.4m from the crop row. θ was used to estimate root zone depletion (D_r). θ was monitored with a frequency of one to three weeks in 2017. Thirty-second neutron counts were used for θ measurements. The soil neutron count data obtained was then divided by average standard neutron count to obtain count ratio. Volumetric water content was obtained by using respective count ratios and the probe's calibration slope and intercept coefficients.

Both NPs were locally calibrated using 22 soil samples extracted during access tube installation in the field in 2017. The typical length of the soil samples used for calibration was about 10 cm with diameter of 4.1 cm. 60-second neutron counts were taken during calibration to increase accuracy. Each measurement of θ from the probe was correlated to volumetric water content obtained from the oven drying (gravimetric) method. The slope and intercept from the field calibration were 0.3132 and -0.1632m^3 m^{-3}, respectively with R^2=0.73 for probe E1; and 0.2869 and -0.1135m^3 m^{-3}, respectively with R^2=0.70 for probe E2. The root mean square error (RMSE) in the calibration process was 0.018 m^3 m^{-3} for probe E1 and 0.019m^3 m^{-3} for probe E2. Both probes needed firmware upgrades and maintenance after the 2017 season. Probe E1 needed new calibration coefficients in 2018 after probe was serviced. Probe E1 was cross-calibrated with probe E2. The new slope and intercept for probe E1 were 0.2766 and -0.1189 m^3m^{-3}, respectively with R^2 = 0.96.

2.3.4. Soil sampling

Soil properties were determined for locations where access tubes were installed (Barker et al., 2018b). The *FC* and *WP* for access tube locations were assumed to represent the entire plot. *FC* was estimated using θ measurements from NP (observational *FC*). *WP* was estimated using correlation with apparent electrical conductivity and laboratory measured *WP* from soil samples.

In 2018, *FC* values for plots were updated using θ measurements taken in 2017. The θ readings from June 19, 2017 and May 12, 2017 were used to update *FC* numbers for plots in the north and south halves of the field, respectively. These two days had θ measurements 2–3 days after a considerable rainfall event, which is suitable for field capacity estimation.

2.4. Water balance components

The water balance was modeled similar to previous research (Barker et al., 2018b). In modeling for the VRI-L, VRI-U, and U treatments, soil was assumed to be at *FC* at the start of each growing season. This assumption was used due to off season recharge of the soil profile from precipitation at the field. Water balance calculations were computed at a daily time step with the end of the day occurring at midnight. All measurements taken during a day were assumed to represent the end of that day. For instance, θ measurements at noon were assumed to represent the midnight θ at the end of that day. The root zone was modeled to grow linearly with time from a specified minimum to a maximum value. The minimum and maximum value of the root zone depth was assumed 0.1m and 1m for both crops, respectively. Initiation of root growth started at the emergence date computed as the day that basal crop coefficient (K_{cb}) first exceeded 0.12, and it was allowed to increase to its peak value when the K_{cb} reached its peak value. Projection of K_{cb} to its peak is discussed below in section 2.5.1.

2.4.1. Effective rainfall

Rainfall data from the installed rain gauges at the field site and the weather station were both used. Data from the rain gauges at the field were used if data from both sources were available, since it was considered more representative of rainfall received by the field than values acquired from the weather station. When recent data from these rain gauges were not downloaded, the weather station data were used for irrigation scheduling purposes. The field rain gauge data were primarily used in the final analysis. The curve number method was used to compute runoff (SCS, 1985). The curve number used for runoff calculations was 80. Runoff was subtracted from rainfall depth to get effective rainfall.

2.4.2. Evapotranspiration

For U plots, single (i.e. mean) K_{cr} were employed to compute crop evapotranspiration (ET_c). Crop coefficients for maize were computed based on Allen and Wright (2002). For soybean, the average daily value of the two single K_{cr} relationships (2007 and 2008) of Irmak et al. (2013) was used. These coefficients were originally developed for Clay Center, Nebraska, which is approximately 160 km southwest of the field. The offseason K_{cr} was assumed to be 0.2. The day-of-year at which mean K_{cr} peaks was estimated early in the season for irrigation forecasting. This estimation was done using 20-year historic daily average values of *GDD* and the previous season's cumulative *GDD* from planting to effective full cover. ET_c were computed following the United Nations' Food and Agricultural Organization's Irrigation and Drainage Paper No. 56 (Allen et al., 1998) using equation:

$$ET_c = ET_r * K_{cr}$$

where ET_c is crop *ET*, ET_r is alfalfa-based reference *ET* and K_{cr} is alfalfa-based crop coefficient.

For VRI treatments, dual K_{cr} were used in SETMI to compute ET_c (Allen et al., 1998). Reflectance-based basal crop coefficients (K_{cbrf}; Neale et al., 2012) were computed based on the soil-adjusted vegetation index (SAVI; Huete, 1988) computed from remote sensing imagery. K_{cbrf} relationships for interpolation from Campos et al. (2017) were used to forecast and estimate K_{cb} on days without remote sensing inputs. In SETMI, dual K_{cr} were computed using equation (Allen et al., 1998):

$$K_{cr} = (K_{cb} * K_s) + K_e$$

where, K_{cb} is basal crop coefficient, K_s is water stress coefficient and K_e is soil evaporation coefficient.

Soil evaporation in SETMI was dampened by 25% for both crops to account for residue present in the field (Barker et al., 2018b). The amount of residue at field was estimated using the line transect method following (Shelton and Jasa, 2009). Residue was estimated through multiple readings at different locations in the field, with transects at about 45° angle to crop rows. Residue percentage was found to be 55% after taking average of 3 readings each from north and south halves of the field.

2.4.3. Stored soil water

As mentioned in section 2.3.3, θ was monitored at seven depths in the soil profile. Depth-weighted average θ was used to represent stored θ in the modeled root zone. Measurements at 15 cm were assumed to represent 0–23 cm, 30 cm to represent 23–38 cm, 46 cm to represent 38–61 cm, 76 cm to represent 61–91 cm, 107 cm to represent 91–122 cm, 137 cm to represent 122–152 cm and 168 cm to represent 152–183 cm. However, the weighted average of θ included only the top 1 m, similar to modeled root zone depth, and was used to update the water balance.

2.4.4. Irrigation

Gross irrigation requirements were calculated from plot-specific water balances. A 9.1-m buffer zone inside the boundary of each plot was used to allow an area for transitions between varying application depths. The irrigation requirements were computed for the inner portion of the plot excluding the buffer area.

Management allowable depletion (*MAD*) was the threshold used for irrigation management. This was the soil water content threshold below which crop water stress was assumed to occur. The *MAD* used for maize was 50% of *AWC* until reproductive stage R5 (dent stage where kernels are partially dented) was reached. Soybean was managed at 55% *MAD* until reproductive stage R2 (full flowering stage where an open flower is present at one of the two uppermost nodes), after which *MAD* was reduced to 50%, considering recommendation of Kranz and Specht (2012). *MAD* was increased to 60% for both crops late in the season (Yonts et al., 2008). Soils were not irrigated to reach *FC*. Irrigating less than *FC* level allowed water from rainfall events to be stored in the root zone. Irrigation was applied to maintain D_r less than *MAD* but not to exceed a specified depth (30.5 mm) less than *MAD*. During real time irrigation management, irrigation requirements were forecasted every week. The maximum irrigation depth applied by the center pivot in a single pass was 30.5 mm. Irrigation depths were split into two or three prescriptions when irrigation requirements exceeded the maximum irrigation depth that could be applied by irrigation system in a single irrigation pass. This methodology for irrigation management is described in detail by Barker et al. (2018b, 2019).

The pivot typically took more than one day to complete a single irrigation event for one half of the field. For water balance calculations, the day when a plot received irrigation was computed based on average pivot travel time. If a plot received irrigation after midnight, it was considered to be irrigated on the next day. Plots were considered to have been irrigated if the pivot passed over the neutron access tube location in the plot. The pivot was assumed to run at a constant speed, though actual speed varied somewhat due to variable application depths. The speed was calculated using the start-stop time and angular distance covered.

Application efficiency was assumed to be 85% to account for losses such as evaporation and wind drift, among others. Gross irrigation was assumed to be the depth of water which was intended to be applied. Net irrigation, the depth which infiltrated into the soil and could be utilized by plants, was the product of the gross irrigation and the application efficiency. After the end of second season of the experiment, the pressure of the pivot was observed to be low. However, we determined that this small change in pressure had a negligible impact on the experiment.

Irrigation prescriptions were adjusted for rainfall if rainfall occurred after irrigation prescription development. If rainfall occurred before applying an irrigation prescription, the prescription was adjusted by reducing the rainfall amount from the prescribed depth. In cases where rainfall happened during an irrigation event, the prescription was not adjusted for rainfall. In these cases, the irrigation events were completed after a rain delay.

2.4.5. Deep percolation

Deep percolation was computed using different methods among the treatments. For the U and VRI-L treatments, an instantaneous *DP* method was used which drained all water in excess of *FC* at the end of the day (Allen et al., 1998). This does not allow D_r to go below 0mm (wetter than field capacity). A decaying function for *DP* (Raes et al., 2017) was used for the new VRI-U treatment in 2018 (Bhatti, 2018). This allowed excess water to stay in the root zone to be used by plants for a few days; D_r could go below 0mm (negative value) meaning that soil water could increase above field capacity temporarily. This method was used during the final analysis for all treatments.

2.5. SETMI modeling for irrigation management

SETMI (Geli and Neale, 2012) was embedded in ESRI's (Redlands, California) geographic information system software ArcGIS v10.4. SETMI was used to compute irrigation requirements for VRI-L and VRIU plots. Refer to Barker et al. (2018a, 2019) for current information on SETMI in addition to the included water balance and TSEB models. Maize and soybean were considered as different fields in the model.

2.5.1. Water balance model

In SETMI, K_{cbrf} values were forecasted using two different methods depending on crop development. The first method was used if the crop development was before full cover. In this method, the K_{cb} curve was projected forward to the day of the year at which K_{cbrf} was expected to reach its peak value based on input imagery. A limit on how late this day could occur was estimated using last season's *GDD* to reach full cover from planting. At least two reflectance images were needed to project the K_{cb} curve to the peak value. The second method was followed after peak K_{cb}. The day when the crop was expected to mature (reach an offseason SAVI value=0.099; Campos et al., 2017) was input in SETMI. This input helps lower K_{cb} value at an appropriate rate after full cover. The offseason K_{cb} value was set to 0.12.

2.5.2. Two source energy balance adjustment

Thermal infrared imagery was input into the TSEB (Norman et al., 1995) within SETMI. The TSEB computed ET_c using the Priestly-Taylor equation to estimate canopy latent heat flux. As in Norman et al. (1995), instantaneous *ET* was calculated using TSEB model and scaled up to daily value. The TSEB adjustment was not made for the VRI-U treatment, since the TSEB model was not adequately tested with UAS thermal imagery. The TSEB was used to adjust ET_c and depletion (Neale et al., 2012) for the VRI-L treatment in both years.

TSEB *ET* was included in SETMI when the fraction of vegetation cover was above 20% for the majority of the field. Crop height and leaf area index, modeled based on Optimized Soil-Adjusted Vegetation Index (OSAVI; Rondeaux et al., 1996) values following Anderson et al. (2004), were adjusted late in the season. This adjustment was made to maintain crop height and leaf area index late in the season.

Crop height and leaf area index images output from TSEB model at full effective cover (peak) were input into model late in the season to maintain peak values.

For VRI-L, TSEB *ET* was used to adjust the K_{cbrf} computed ET_c on each day a thermal image was input into SETMI. The adjustment was weighted based on the Kalman gain factor (*W*). The *W* can range from 0 to 1 to change the weight of TSEB *ET* in calculating the resulting ET_c after adjustment (Neale et al., 2012).

$$ET^{A}_{WB} = ET^{B}_{WB} + W\,(ET_{TSEB} - ET^{B}_{WB}) \quad (1)$$

where ET^{A}_{WB}, ET^{B}_{WB} are crop *ET* from water balance with and without adjustment using TSEB *ET*, respectively, and ET_{TSEB} is *ET* calculated by TSEB. We used *W* of 0.56 in computing actual *ET* (Barker et al., 2018a).

The TSEB *ET* could also update the soil water balance by adjusting the modeled depletion through the K_s. In cases when the $ET_{TSEB} < ET^{B}_{WB}$, the K_s was recomputed and the depletion for the beginning of the day was also updated. However, in the case when $ET_{TSEB} \geq ET^{B}_{WB}$, and K_s=1, then no adjustment was made to the modeled depletion value.

2.5.3. Adjustment using measured soil water content

The output depletion from SETMI was adjusted using θ measurements from NP. Mean depletion adjustment was used to adjust modeled depletion in 2017 and 2018. Four plots from the VRI-L and VRI-U treatments were selected for each of the two crop-year combinations. These plots had θ values close to the 0th, 33rd, 66th, and 100th percentiles of the range of θ values on a measurement day among respective VRI-L and VRI-U plots. The selected dates were the most recent dates at which θ measurements were available at that time of selecting plots. The model was updated as:

$$D_{adj} = D_{mo} + (\bar{D}_{ms} - \bar{D}_{mo})$$

where D_{adj} is the adjusted depletion using measured soil water content from NP, D_{mo} is modeled depletion, $\bar{D}_{ms}$ is mean of measured depletion for 4 plots and $\bar{D}_{mo}$ is mean of modeled depletion for 4 plots. This adjustment was made on each NP measurement day in 2017 and 2018.

2.6. Data analysis

The total prescribed gross irrigation depth was compared between treatments. Treatments were also compared using various response variables, including ET_a, crop yield, *DP*, change in soil water storage (*ΔSW*), irrigation water use efficiency (*IWUE*), evapotranspiration water use efficiency (*ETWUE*), and crop water use efficiency (*CWUE*). The various efficiencies were computed following Djaman and Irmak (2012) as:

$$IWUE = (Y_i - Y_d) \div I_i$$

$$ETWUE = \quad (Y_i - Y_d) \div (ET_i - ET_d)$$

$$CWUE = Y \div ET_a$$

where *IWUE, ETWUE and CWUE* are expressed in kg $ha^{-1}mm^{-1}$, *Y* is dry yield (kg ha^{-2}), *I* is applied irrigation depth (mm), and ET_a is actual crop evapotranspiration (mm). Subscripts *i* and *d* represent variables corresponding to irrigation treatment *i*, and dryland treatment *d*, respectively.

2.6.1. Computation of response variables

Seasonal water balances were modeled for each plot to compute each of these variables. Analysis was performed between the first and last day of NP measurements. SETMI was used to perform the water balance for the final analysis as well as in-season management. The measurement period in 2017 was from April 18 to September 22 for maize and from May 9 to September 29 for soybean. The measurement period in 2018 was from April 23 to September 22 for maize and from May 8 to September 18–19 for soybean. The last θ measurements for soybean in 2018 were taken in two days due to a rainfall event happening later in the day on September 18. Rainfall on September 18 was not included in the water balance calculations for plots with the last θ readings on September 18 since θ readings were taken before the rainfall event for these plots. However, this rainfall event was included for plots with last θ readings on September 19.

As discussed above, a root zone depth of 1m was used during irrigation management. During final analysis, the root zone depth was considered to be constant at 1.22m for both crops. Weighted average of θ readings down to 1.22m depth were used to represent soil water status on measurement dates.

Landsat 7 and 8 imagery was used in SETMI for analysis in 2017. Due to sparse Landsat imagery in 2018, UAS imagery was used in the final analysis to run seasonal water balances and compute response variables in 2018. Peak SAVI values were based on imagery (no forecasting). For soybean, no end-of-season forecasted SAVI value was input late in the 2017 fin. l analysis. Projected end SAVI values were input for maize due to lack of imagery close to end of season in both years. For soybean in 2018, projected end SAVI was also used. The projected end SAVI was estimated based on visual observations of crop maturity close to the end of the season.

2.6.2. Yield processing

Crop yield was measured using yield monitoring equipment on harvesters. Yield data was filtered and cleaned using Yield Editor software version 2.0 (Agricultural Research Service, United States Department of Agriculture). The filtered clean data was checked using the mean yield (weight per unit area) reported for weighing grain carts. Plots were excluded from analysis if processed plot yield data points were less than 20 for maize and less than 25 for soybean within a 12.1m buffer within each plot in 2017. Threshold for excluding plots from 2018 analysis was less than 30 yield data points for both crops.

The yield analysis was done on the computed dry mass of crop grain yield. Mass of the moisture (using yield monitor measured moisture) present in grains during harvest was removed from grain mass while executing calculations for yield analysis.

2.6.3. Statistical analysis

Statistical analyses were performed to test the hypothesis that there will be no significant differences in yield and ET_a between treatments. Multivariate analysis of variance (MANOVA) and univariate analysis of variance (ANOVA) were performed to study treatment and blocking effects on the response variables. Wilks' lambda statistic was used to study results from MANOVA tests. SAS 9.4 (SAS Institute, Inc., Cary, NC) software was used to compute statistical analyses on the data.

MONOVA tests and partial correlations between response variables were performed using PROC GLM. ANOVA using PROC GLIMMIX was run and type III sum of squares and cross-products were calculated. Blocking was considered to be a fixed effect when these tests were performed. Analyses on applied seasonal irrigation and response variables were performed separately. The least squares means were tested at a 5% significance level. The correlations were tested at a significance level of 10%.

2.7. Eliminated data

In 2017, two plots (in VRI-L and R treatments) were not used in the analyses for maize. The eliminated plot in VRI-L had an accidental spill of water on the neutron access tube which may have resulted in erroneous soil water status in that plot. This plot was also used to correct the model using θ measurements. The spill of water occurred after irrigation prescriptions were applied in 2017. The excluded plot in R was due to low yield data points. No plot was excluded for soybeans.

In 2018, five plots in soybean (1–2 in each treatment) and one plot in maize (in the U treatment) were excluded from final analysis due to insufficient yield data points for these plots.

3. Results and discussion

3.1. Soil properties

Estimates of *FC* and *WP* from Barker et al. (2018b) were used for the 2017 growing season. The range of *FC* values was from 0.37 to 0.43m^3m^{-3} for north half and 0.37 to 0.41m^3m^{-3} for south half. *WP* values ranged from 0.17 to 0.21m^3m^{-3} for north and 0.18 to 0.20m^3m^{-3} for south. As a result, *AWC* values ranged from 0.17 to 0.25m^3m^{-3} for the north and 0.17 to 0.24m^3m^{-3} for the south.

The new *FC* values used in 2018 ranged from 0.37 to 0.45m^3m^{-3} for the north plots and 0.38 to 0.44m^3m^{-3} for the south plots. The new *FC* numbers, in general, were greater than the values used in 2017. This resulted in an increase in *AWC* for most of the plots, which had a small effect on soil water balance calculations.

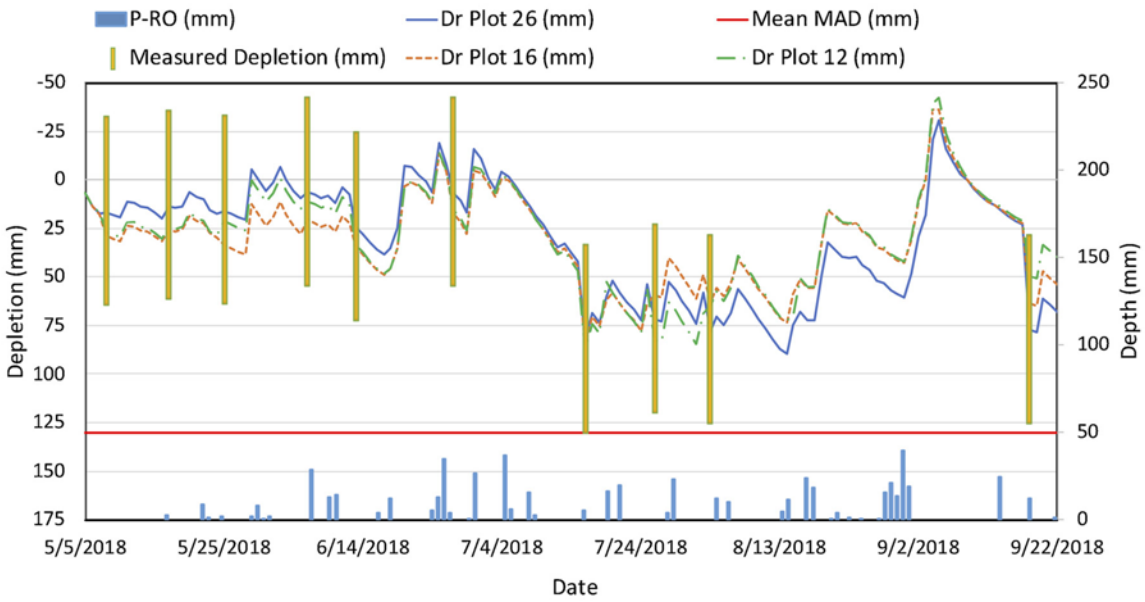

Fig. 2. Seasonal depletion for three plots in VRI-U for soybean in 2018. All values except net rainfall amount (P-RO) are plotted on left vertical axis in reverse direction. Days with measured depletion are shown in vertical yellow lines.

3.2. Spatial variability in seasonal depletion

Fig. 2 depicts spatial variability in soil water content by showing D_r throughout the season for three plots in the soybean VRI-U treatment in 2018. These plots belong to different soil blocks (from 6 blocks in north half). Mean *MAD* shown in Fig. 2 was calculated as average value of respective *MAD* values for these three plots. Plots 12, 16, and 26 (Fig. 2) were prescribed with a total gross irrigation of 117, 91, and 107 mm, and had mean dry yield of 3.8, 3.1, and 3.1 Mg ha^{-1}, respectively. Plot 12, which had the highest seasonal irrigation, tended to have the greatest depletion (Fig. 2) during the dry portion of the season when irrigation was needed (late July and early August).

3.3. Mean total gross prescribed irrigation depth

In this section, treatment differences for I_p applied to the crop during the growing season are discussed. In 2017, I_p for plots under the VRI-L treatment ranged from 56 to 107mm (**Fig. 3**). Plots under U treatment received equal I_p (**Table 2**). For maize, I_p was 77mm

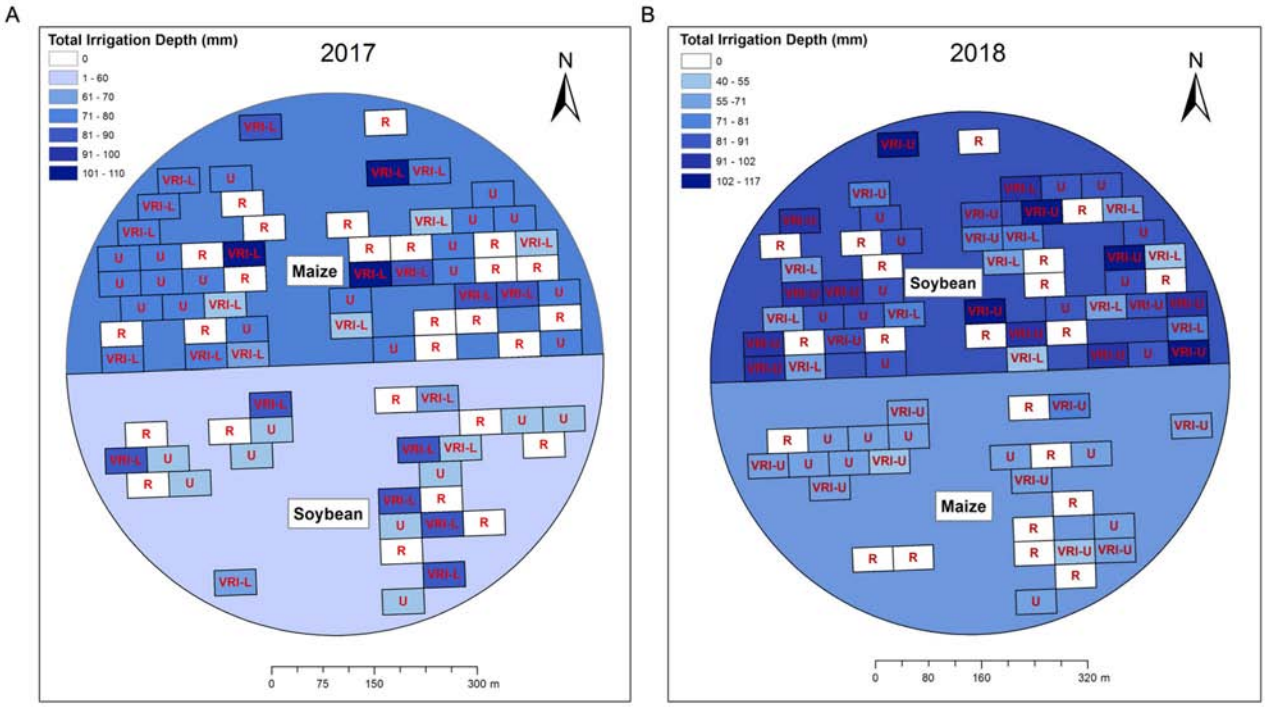

Fig. 3. Total mean prescribed irrigation depth (I_p) for each plot in 2017 and 2018.

Table 2. Mean total seasonal gross irrigation prescribed (*Ip*) for treatments in 2017 and 2018.

2017			*2018*		
Treatment	*Mean [a] ± SE [b] (mm)*	*DF [c]*	*Treatment*	*Mean ± SE (mm)*	*DF*
Maize			***Maize***		
VRI-L	76.5 ± 3.3	12	VRI-U	63.8 ± 1.9	22
U	76.2		U	66.0	
R	0		R	0	
Soybean			***Soybean***		
VRI-L	76.2 ± 4.4	6	VRI-L	70.3 ± 2.8	40
U	50.8		VRI-U	97.6 ± 2.3	40
R	0		U	91.4	
			R	0	

a. Least squares means of different response variables.
b. Standard error of the means.
c. Degrees of freedom.

for VRI-L treatment and 76mm for the U treatment. Treatment differences were not found to be significant. Contrary to these results, Barker et al. (2018b) found that I_p applied for VRI-L treatment was significantly greater than the U treatment in maize for this site during their two-year field study in 2015 and 2016. Their study did not include θ measurements in the model and a different value of W was used for incorporating TSEB ET in the model. In our study, model adjustments using measured θ often decreased depletion in the model which likely decreased the irrigation requirements prescribed. For soybean, I_p for the U treatment (51 mm) was significantly lower than I_p for the VRI-L (76 mm) treatment. The range of I_p depth was 56–87mm for plots under the VRI-L treatment.

For the 2018 maize crop, I_p for VRI-U (64 mm) and U (66 mm) treatments were not significantly different from each other. For soybean, I_p was 98mm for VRI-U, 91mm for U, and 70mm for VRI-L. Significant differences in soybean were observed between all treatments. Less water was prescribed to the VRI-L treatment signifying a reduction in water withdrawals over the U and VRI-U treatments. A small difference in I_p was observed between the VRI-U and U treatments. We acknowledge this difference is small and not practically meaningful. For soybean in 2018, VRI-U had larger I_p than VRI-L. VRI-U had larger estimated mean ET_c over VRI-L, which may have led to increased irrigation requirements in VRI-U.

3.4. Correlation among response variables

In 2017, we found significant correlation between ΔSW and ET_a for both crops ($P < 0.0001$). Other significant correlations for maize included ET_a with yield ($P=0.003$), ET_a with DP ($P < 0.0001$), and yield with DP ($P=0.013$). Other significant correlations for soybean were between ΔSW and DP ($P=0.016$), and ΔSW and yield ($P=0.039$). In 2018, significant correlations for maize were observed between ET_a with DP ($P < 0.0001$), ΔSW and ET_a ($P < 0.0001$), ET_a with yield ($P=0.002$), and ΔSW & yield ($P < 0.0001$). For soybean, only significant correlation was observed between DP and ET_a ($P < 0.0001$). Based upon these significant correlations, MANOVAs were computed.

3.5. MANOVA and univariate ANOVA test results

3.5.1. MANOVA test

In the U treatment, irrigation was managed based on soil with lower 10th percentile of *AWC*; hence, most parts of the field were sufficiently irrigated to prevent yield reduction. In years with normal rainfall amounts, fields dependent solely on rainfall produce large yields in proximity to the study site. The results of the tests for the 2017 and 2018 data are discussed below.

We found that treatments had a significant overall effect on response variables for both crops in 2017 and 2018 ($P < 0.0001$). Hence, the data provided enough evidence to reject the null hypothesis that there were no treatment differences. The blocking effect was also significant for both crops in 2017 ($P < 0.0001$ for maize and $P=0.0265$ for soybean in 2017). Univariate ANOVAs were computed after MANOVA results were found to be significant. In 2018, the blocking effect was not significant for maize.

3.5.2. Univariate ANOVA test

Individual univariate ANOVAs for both crops were performed to study differences in response variables for all treatments. Results for four response variables: ET_a, *DP*, Δ*SW*, and yield, are discussed. All effects were tested at a 5% significance level. Overall, the treatment had a significant effect on ET_a for both crops in 2017 ($P=0.0001$). We were able to reject the null hypothesis when ET_a was compared for these cases. Significant differences were also found in Δ*SW* and yield due to treatment effect for maize in 2017.

3.5.3. Least squares means of response variables

Table 3 is a summary of estimated least squares means from the ANOVAs for various response variables in each treatment for all crop year combinations. For maize in 2017, mean yield ranged from 11.6–12.2 Mg ha^{-1}. The minimum and maximum plot yields were 8.3 and 13.4 Mg ha^{-1}, respectively. The minimum yield was found in one of the R plots. Significantly greater maize yield was observed for VRI-L (12.2 Mg ha^{-1}) treatment than for the R (11.6 Mg ha^{-1}) treatment. We may attribute increased yields as compared to R plots to be due to irrigation applied to the VRI-L treatment. Mean yield for the U (12

Table 3. Least squares means for different response variables and multiple ranges groupings.

Treatment	*ET_a (mm)* *M*±SE†*	*DP (mm)* *M ± SE*	*ΔSW (mm)* *M ± SE*	*Yield (Mg ha^{-1})* *M ± SE*
Maize 2017				
VRI-L	552 ± 5.7 a‡	52.3 ± 3.1 a	−21.0 ± 4.5 a	12.2 ± 0.18 a
U	557 ± 5.5 a	53.1 ± 3.0 a	−26.4 ± 4.3 a	12.0 ± 0.17 ab
R	496 ± 5.7 b	50.5 ± 3.1 a	−39.3 ± 4.5 b	11.6 ± 0.18 b
Soybean 2017				
VRI-L	545 ± 9.2 a	105 ± 4.9 a	−67.3 ± 9.9 a	4.01 ± 0.07 a
U	511 ± 9.2 b	106 ± 4.9 a	−59.3 ± 9.9 a	4.07 ± 0.07 a
R	477 ± 9.2 c	111 ± 4.9 a	−81.5 ± 9.9 a	4.06 ± 0.07 a
Maize 2018				
VRI-U	597 ± 9.3 a	40.4 ± 6.5 a	−11.7 ± 5.1 a	12.0 ± 0.18 a
U	595 ± 9.9 a	45.2 ± 6.8 a	−12.7 ± 5.4 a	12.2 ± 0.19 a
R	531 ± 9.3 b	39.6 ± 6.5 a	−8.5 ± 5.1 a	12.1 ± 0.18 a
Soybean 2018				
VRI-L	550 ± 9.7 a	43.6 ± 8.3 a	−37.6 ± 5.9 a	3.38 ± 0.08 a
VRI-U	567 ± 7.8 a	54.5 ± 6.7 a	−38.8 ± 4.7 a	3.42 ± 0.06 a
U	565 ± 10.4 a	48.9 ± 8.9 a	−43.2 ± 6.3 ab	3.28 ± 0.08 a
R	505 ± 9.7 b	19.6 ± 8.4 b	−57.4 ± 5.9 b	3.41 ± 0.08 a

* Least squares means of different response variables.
† Standard error of the means.
‡ Letters denote multiple range groupings.

Mg ha^{-1}) treatment was greater than the R (11.6 Mg ha^{-1}), but it was not significantly different. The mean yield for different treatments in soybean ranged between 4 and 4.1 Mg ha^{-1}. Plot yield ranged from 3.4 to 4.4 Mg ha^{-1}. Significant differences in soybean yield were not found among treatments. This may be a result of having adequate water availability from rainfall for soybean. Thus, more water in irrigated plots did not increase the yield for soybean in 2017.

No significant differences in maize and soybean yield were observed in 2018. All treatments performed similar to each other for both crops. Converse to results observed in 2017, the R treatment performed similarly to the irrigated treatments. This could be attributed to better distribution of rainfall events during the vegetative stages of crops in 2018. The range of mean maize yield was 12.0 to 12.2 Mg ha^{-1}. Mean yield for the VRI-U and R treatments was 12 Mg ha^{-1} and 12.1 Mg ha^{-1}, respectively. Rainfall in 2018 may have been adequate to keep the crop free from significant water stress and to produce adequate yield when compared to other irrigated treatments. Mean

soybean yield in 2018 ranged from 3.3 to 3.4 Mg ha^{-1}. Minimum mean soybean yield was found in the U treatment (3.3 Mg ha^{-1}).

As discussed above, there were treatment differences found in mean seasonal ET_a for both crops. In 2017, the R (496 mm) treatment had significantly lower mean ET_a than other treatments for maize. As expected, ET_a was correlated with yield for the maize crop in 2017. However, ET_a and yield were not correlated for soybean in 2017. Larger ET_a in the VRI-L and U treatments for soybean could be attributed to overestimation of ET_a, possibly through under estimation of *DP* and runoff. Mean ET_a in soybean was largest for VRI-L (545 mm) and smallest for R (477 mm).

In 2018, mean ET_a for maize was larger for irrigated treatments than for the R treatment. However, this trend was not observed in maize yield. Mean ET_a was not significantly different among the VRI-L (597 mm) and U (595 mm) treatments. The R (531 mm) had significantly lower mean ET_a than VRI-L and U. For soybean, mean ET_a for VRI-U and U was significantly greater than R and VRI-L. Mean ET_a was 565mm for U and 567mm for VRI-U. The R had significantly less ET_a than the other treatments. These *ET* differences also did not result in differences in yield among treatments. Reasons could be attributed to overestimation of ET_a.

It was originally hypothesized that VRI would result in reduced pumping for irrigation but would not reduce consumptive use (ET_c), since both VRI and U would be managed for a full yield and yield is closely correlated to *ET*. However, in the one crop-year combination when VRI reduced I_p (2018 soybean), there was a corresponding reduction in consumptive use (15 mm) without a negative impact on yield (**Table 3**). This would result in a consumptive use ratio ($\Delta ET_a/\Delta I_p$) of 0.6, although the difference in ET_a was not statistically significant. It is expected that, if the U treatment had represented common practice instead of good irrigation scheduling, I_p for U would have been much higher than I_p for VRI, and the consumptive use ratio would have been small. Future research should include additional treatments and sites to further explore the impact of VRI on consumptive use.

Computed mean *DP* was only significantly different for soybean in 2018. For soybean in 2018, mean *DP* was lowest for R (19.6 mm). We did not find any significant reduction in *DP* with VRI treatments in comparison to the U treatment. Mean ΔSW was different among treatments for maize in 2017 and soybean in 2018. In both cases, R

had the lowest Δ*SW* compared to other treatments. This indicates that less water was available in the root zone soil layer at the end of the season for R in these cases.

Three efficiencies were computed to compare the performance of the irrigation treatments (**Table 4**). In 2017, *IWUE* for maize varied from 6.6 kg $ha^{-1}mm^{-1}$ for U to 8.4 kg $ha^{-1}mm^{-1}$ for the VRI-L treatment. *IWUE* and *ETWUE* for soybean in 2017 and for both crops in 2018 were small and were not presented since differences in yield were not significant. In 2017, maize had *ETWUE* values of 11 kg $ha^{-1}mm^{-1}$ for VRI-L, and 8 kg $ha^{-1}mm^{-1}$ for U. *CWUE* in 2017 ranged from 21.5 kg $ha^{-1}mm^{-1}$ for the U treatment to 23.4 kg $ha^{-1}mm^{-1}$for the R treatment for maize. *CWUE* ranged from 7.3 kg $ha^{-1}mm^{-1}$ for the VRIL treatment to 8.6 kg $ha^{-1}mm^{-1}$ for the R treatment for soybean. In 2018, R had the greatest *CWUE* among treatments with 22.6 kg $ha^{-1}mm^{-1}$ for maize and 6.7 kg $ha^{-1}mm^{-1}$ for soybean.

Table 4. Water use efficiencies for treatments for maize and soybean in 2017 and 2018.

Treatment	*IWUE* (kg $ha^{-1}mm^{-1}$)	*ETWUE* (kg $ha^{-1}mm^{-1}$)	*CWUE* (kg $ha^{-1}mm^{-1}$)
Maize 2017			
VRI-L	8.4	11	22.1
U	6.6	8	21.5
R	n/a	n/a	23.4
Soybean 2017			
VRI-L	–[a]	–	7.3
U	–	–	8
R	n/a	n/a	8.6
Maize 2018			
VRI-U	–	–	20
U	–	–	20.4
R	n/a	n/a	22.6
Soybean 2018			
VRI-L	–	–	6.2
VRI-U	–	–	6
U	–	–	5.8
R	n/a	n/a	6.7

a. Differences in yield were not significant.

3.6. Modeling differences using UAS and Landsat imagery

3.6.1. Spatial resolution

Landsat 7 and 8 capture images at a 30-m ground resolution for multispectral imagery (green, red, and near-infrared bands), and 100-m and 60-m resolution for thermal infrared imagery taken from Landsat 8 and 7, respectively (USGS, 2018, 2019). Modeling water balance components using these resolutions may not be sufficient to study spatial variability at a sub-field scale. The spatial resolution of remote sensing imagery has significant impact on estimation of energy balance components using energy balance models such as METRIC, especially in heterogeneous systems (Ramirez-Cuesta et al., 2019). This can be observed in **Fig. 4**(A) and (B), where a Landsat thermal infrared image processed to 30-m resolution (USGS, 2019) is shown underlying the experimental plots. The color in the plots depicts the values of SAVI. Fig. 4(B) is an image of modeled SAVI for 5 experimental plots. Additionally, the resolution of Landsat satellite imagery was coarse for the plot size used in the study. This caused mixing of pixels, introducing considerable interference effects from neighboring areas around a plot.

Fig. 4(C) and (D) are images of SAVI values computed using UAS imagery for the same set of plots as in Fig. 4(A) and (B). The UAS thermal infrared imagery in Fig. 4(C) and (D) were processed to a ground resolution of 1 m. The enhanced resolution was useful for closely studying spatial variability as depicted in Fig. 4(D). The UAS thermal infrared image clearly demarcates an area of high temperatures which crosses some parts of the plots. This may identify field characteristics more precisely and, consequently, help in developing precise VRI prescription maps. The minimum SAVI value presented in Fig. 4(C) and (D) was 0.3, which was much lower than the lowest SAVI value for the Landsat case (0.57) as a consequence of pixel mixing. The maximum computed SAVI values in both Landsat and UAS cases were similar (0.77) corresponding to well-developed homogeneous areas. The relatively coarse Landsat resolution smooths the effect of high temperature (low vegetation) areas with adjacent cool areas (high vegetation density), making it more difficult to study variable field characteristics. This comparison of mapping SAVI values was achieved using Landsat and UAS imagery taken on different days with only one overlap date

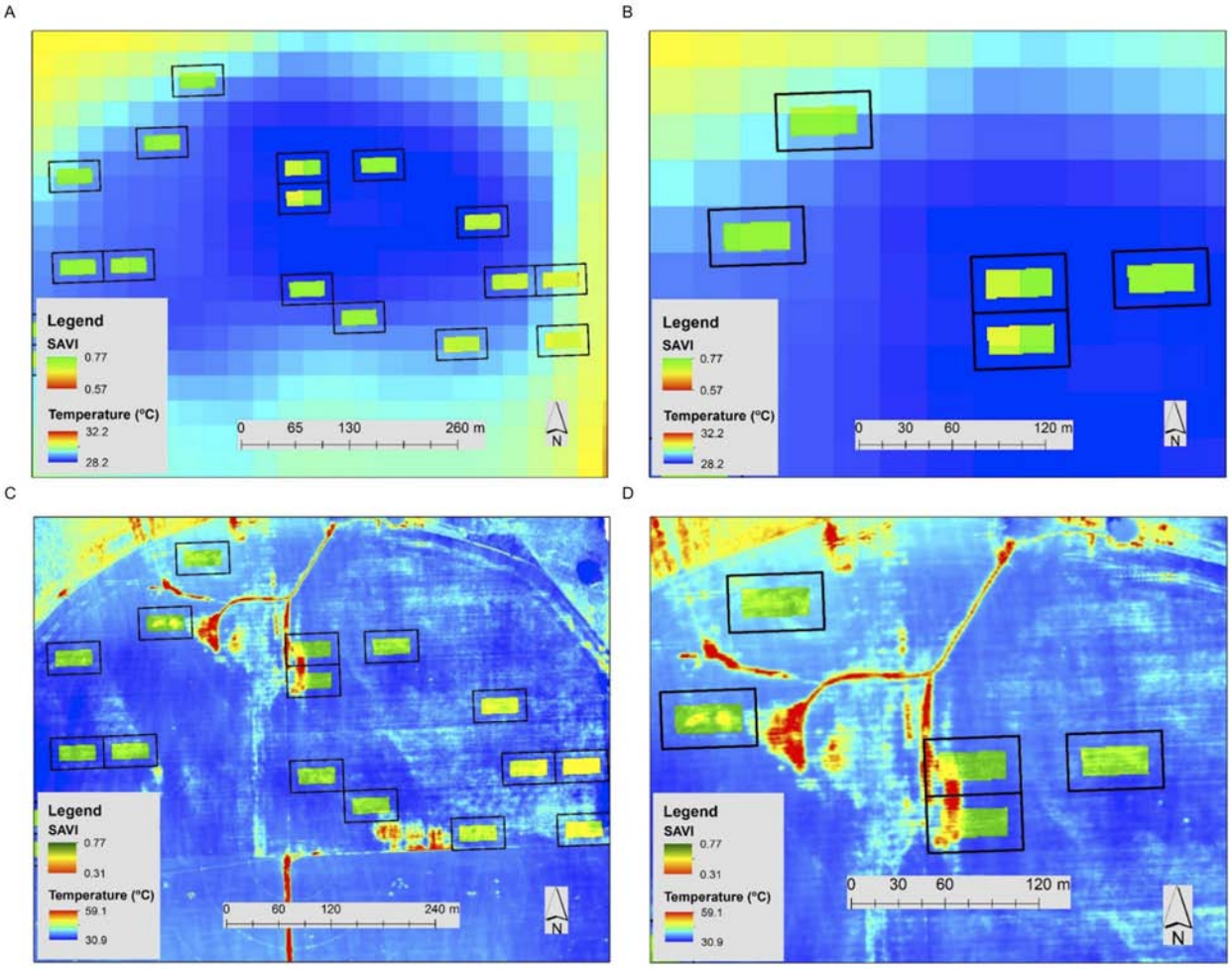

Fig. 4. Computed SAVI (green and yellow) within the buffer of experimental plots (black rectangles) overlain on thermal infrared canopy temperature for low- and high-resolution imagery. (A) is the zoomed out view and (B) is the zoomed in view for 19 July, 2018 using Landsat 8 imagery. (C) is the zoomed out view and (D) is the zoomed in view for 11 July, 2018 using UAS imagery.

between two datasets. This did not affect the analysis because SAVI was interpolated between remote sensing inputs and SAVI from same date is shown for both Landsat and UAS cases in Fig. 4.

3.6.2. Temporal resolution

Landsat 7 and 8 pass over a location every 16 days with an offset of 8 days between the two satellites. The frequency may be sufficient for irrigation scheduling purposes. Landsat images were not usable in the model on days with high cloud cover. One UAS image was taken on a

Landsat overpass day (July 11) in 2018. In the study for year 2018, no cloud free Landsat images were acquired from the mid-to-late season. Another issue with using Landsat 7 is missing data strips in the imagery from the scan line correction problem (USGS, 2018).

The problem of missing data could be addressed by using a UAS to capture remote sensing images (Woldt et al., 2018). The UAS can be flown to capture imagery on sunny and low wind days (Maguire, 2018). The UAS data collection was successful for year 2018 and images were collected for most weeks during the growing season. This promising aspect of UAS imagery could be utilized for reliable VRI management.

3.7. Challenges in using UAS thermal infrared imagery in the TSEB model

3.7.1. Updated relations for computing TSEB parameters

SETMI used relationships for computing parameters for TSEB, including fraction of cover (Li et al., 2005; Barker et al., 2018a), plant height, and leaf area index (Anderson et al., 2004). These coefficients are applicable for Landsat imagery and are crop-specific. Errors may be induced in estimation of *ET* components if these Landsat specific coefficients are used for TSEB modeling using UAS imagery. These relationships must be updated before using UAS imagery with TSEB model. This was the primary reason for exclusion of TSEB model adjustments from the UAS treatment. New relationships have been developed for UAS imagery (Maguire, 2018). Future work is required to validate TSEB *ET* using UAS imagery with ground truth data from a direct *ET* measurement, such as eddy covariance flux *ET* data.

3.7.2. Thermal infrared imagery calibration

In this study, point measurements of mounted Apogee SI-111 infrared thermometers (Apogee Instruments, Inc., Logan, Utah, USA) were compared to respective pixels in the UAS-collected raw thermal infrared imagery. The mounted infrared thermometers were installed in 12 locations in the field. The comparison indicated that temperature from mounted sensors was lower than UAS imagery temperature in a majority of cases. Raw thermal infrared imagery from UAS resulted in an error larger than 4 K when atmospheric corrections were not applied to the imagery (Berni et al., 2009). A few potential methods for

calibration of UAS thermal imagery are discussed in Maguire (2018). Ongoing work for calibration seems promising for use of thermal infrared imagery from UAS in the SETMI model in coming years.

4. Summary and conclusions

A study of VRI was conducted in a maize and soybean field in eastern Nebraska using UAS imagery as well as satellite imagery. VRI treatments were compared with U and R treatments in terms of crop yield and water response. In 2017, significantly larger maize yield was observed in the VRI-L treatment than the R treatment, with mean yields ranging from 11.6 to 12.2 Mg ha^{-1}. The increase in yield in VRI-L treatment versus R was attributed to irrigation. For soybean 2017, mean yield ranged from 4 to 4.1 Mg ha^{-1}, with no significant yield increases due to irrigation applications. In 2018, no significant yield differences were found among treatments for maize or soybean. In the one crop-year combination that had significant yield differences (maize 2017), *IWUE* for VRI-L (8.4 kg $ha^{-1}mm^{-1}$) was larger than the U treatment (6.6 kg $ha^{-1}mm^{-1}$).

The I_p was different among U and VRI treatments for soybean in 2017. The I_p for the VRI-L treatment (76 mm) was significantly greater than the U treatment (51 mm). Significant differences were not found for maize in 2017. In 2018, VRI-L had lower I_p than the other irrigated treatments in soybean. The I_p was not significantly different between U and VRI-U in maize in 2018. It is evident that the VRI treatments were able to produce adequate yields as compared with the U treatment and VRI-L performed significantly better than the other treatments for maize in 2017. We found a significant reduction in I_p for VRI-L treatment in soybean in 2018. Hence, significant water withdrawal reduction was observed for one case in the study. One reason for the small differences in I_p is that the U treatment represented good irrigation scheduling instead of common practice, which often results in overirrigation.

The field research has led to the continued development of SETMI as a decision support tool for making VRI prescription maps. The finer temporal and spatial resolution of UAS imagery compared to Landsat imagery was beneficial for modeling purposes. The VRI-U treatment managed using multispectral UAS imagery produced yield similar to

other treatments and used similar mean I_p compared to the U treatment. This signifies that VRI-U could adequately manage irrigation similar to the VRI-L and U treatments, and there is potential for improving modeling using UAS imagery in the future. While UAS thermal imagery is often used to identify relative patterns in canopy temperature, using UAS to determine accurate temperatures for surface energy balance modeling remains a challenge. Overall, VRI using SETMI could be adopted for irrigation management to produce adequate yields in subhumid climates with a reduction in water withdrawals in some scenarios. Further studies are required to implement VRI more accurately and to evaluate the benefits of VRI relative to the costs and labor requirements.

Declaration of Competing Interest — The authors declare that they have no known competing financial interests or personal relationships that could have appeared to influence the work reported in this paper.

Acknowledgments — The funding for this research was provided by Graduate Student Support from the Robert B. Daugherty Water for Food Global Institute at the University of Nebraska, a USGS 104(b) grant from the Nebraska Water Center, and a grant from the USDA NIFA Agricultural and Food Research Initiative (Award Number 2017-67021-26249). Additional support was received from the Hatch Act (USDA NIFA, Accession Number 1009760) and the Department of Biological Systems Engineering at the University of Nebraska–Lincoln. The authors thank Mr. Mark Schroeder and his team from the University of Nebraska's Eastern Nebraska Research and Extension Center for their cooperation and help with field operations. We also thank Alan Boldt, Jasreman Singh, Isabella Possignolo Presotto, Julienne Irihose, Rene Francis Simbi Mvuyekure, Troy Nelson, Joviale Uwase, and Tonny Ruhinda for their help in collecting data and field work. We also acknowledge personnel from the Biological Systems Engineering Department at University of Nebraska for their support and help throughout the experiment. Weather data were provided by the Nebraska Mesonet and the Nebraska State Climate Office through the High Plains Regional Climate Center.

References

Allen, R.G., Pereira, L.S., Raes, D., Smith, M., 1998. Crop evapotranspiration: guidelines for computing crop water requirements. Irrigation and Drainage Paper 56. Food and Agriculture Organization of the United Nations, Rome, Italy.

Allen, R.G., Wright, W.C., 2002. Conversion of Wright (1981) and Wright (1982) Alfalfa-Based Crop Coefficients for Use with the ASCE Standardized Penman-Monteith Reference Evapotranspiration Equation. Tech. Note-USDA-ARS, Kimberly, Id.

Allen, R.G., Tasumi, M., Trezza, R., 2007. Satellite-based energy balance for mapping evapotranspiration with internalized calibration (METRIC)-model. J. Irrig. Drain. Syst. 133, 380–394.

Anderson, M.C., Neale, C.M.U., Li, F., Norman, J.M., Kustas, W.P., Jayanthi, H., Chavez, J.L., 2004. Upscaling ground observations of vegetation water content, canopy height, and leaf area index during SMEX02 using aircraft and Landsat imagery. Remote Sens. Environ. 92 (4), 447–464. https://doi.org/10.1016/j.rse.2004.03.019

Barker, J.B., Neale, C.M.U., Heeren, D.M., Suyker, A.E., 2018a. Evaluation of a hybrid reflectance-based crop coefficient and energy balance evapotranspiration model for irrigation management. Trans. ASABE 61, 533–548. https://doi.org/10.13031/trans.12311

Barker, J.B., Heeren, D.M., Neale, C.M.U., Rudnick, D.R., 2018b. Evaluation of variable rate irrigation using a remote-sensing-based model. Agric. Water Manage. 203, 63–74. https://doi.org/10.1016/j.agwat.2018.02.022

Barker, J.B., Bhatti, S., Heeren, D.M., Neale, C.M.U., Rudnick, D.R., 2019. Variable rate irrigation of maize and soybean in West-Central Nebraska under full and deficit irrigation. Front. Big Data 2 (34). https://doi.org/10.3389/fdata.2019.00034

Barsi, J.A., Barker, J.L., Schott, J.R., 2003. An atmospheric correction parameter calculator for a single thermal band earth-sensing instrument. IEEE International Geoscience and Remote Sensing Symposium 2003 2–4. https://doi.org/10.1109/IGARSS.2003.1294665

Bastiaanssen, W.G.M., Menenti, M., Feddes, R.A., Holtslag, A.A.M., 1998. A remote sensing surface energy balance algorithm for land (SEBAL): 1. Formulation J Hydrol. 212, 198–212.

Berni, J.A., Zarco-Tejada, P.J., Suarez, L., Fereres, E., 2009. Thermal and narrowband multispectral remote sensing for vegetation monitoring from an unmanned aerial vehicle. IEEE Trans. Geosci. Remote. Sens. 47 (3), 722–738.

Bhatti, S., 2018. Variable Rate Irrigation Using a Spatial Evapotranspiration Model With Remote Sensing Imagery and Soil Water Content Measurements. M.S. Thesis. Department of Biological Systems Engineering, University of Nebraska, Lincoln, Nebraska. https://digitalcommons.unl.edu/biosysengdiss/83/

Brunsell, N.A., Gillies, R.R., 2002. Incorporating surface emissivity into a thermal atmospheric correction. Photogramm. Eng. Remote Sens. 68, 1263–1269.

Campos, I., Neale, C.M.U., Suyker, A.E., Arkebauer, T.J., Goncalves, I.Z., 2017. Reflectance-based crop coefficients REDUX: for operational evapotranspiration estimates in the age of high producing hybrid varieties. Agric. Water Manage. 187, 140–153. https://doi.org/10.1016/j.agwat.2017.03.022

Daccache, A., Knox, J.W., Weatherhead, E.K., Daneshkhah, A., Hess, T.M., 2015. Implementing precision irrigation in a humid climate - recent experiences

and ongoing challenges. Agric. Water Manage. 147, 135–143. https://doi.org/10.1016/j.agwat.2014.05.018

Djaman, K., Irmak, S., 2012. Soil water extraction patterns and crop, irrigation, and evapotranspiration water use efficiency of maize under full and limited irrigation and rainfed settings. Trans. ASABE 55, 1223–1238. https://doi.org/10.13031/2013.42262

Evans, R.G., LaRue, J., Stone, K.C., King, B.A., 2013. Adoption of site-specific variable rate sprinkler irrigation systems. Irrig. Sci. 31 (4), 871–887. https://doi.org/10.1007/s00271-012-0365-x

Finkenbiner, C.E., Franz, T.E., Gibson, J., Heeren, D.M., Luck, J.D., 2018. Integration of hydrogeophysical datasets for improved water resource management in irrigated systems. Precis. Agric. https://doi.org/10.1007/s11119-018-9582-5

Geli, H.M.E., Neale, C.M.U., 2012. Spatial EvapoTranspiration Modelling Interface (SETMI). Remote Sensing and Hydrology. pp. 171–174.

Hedley, C.B., Yule, I.J., 2009. A method for spatial prediction of daily soil water status for precise irrigation scheduling. Agric. Water Manag. 96 (12), 1737–1745. https://doi.org/10.1016/j.agwat.2009.07.009

Irmak, S., Odhiambo, L.O., Specht, J.E., Djaman, K., 2013. Hourly and daily single and basal evapotranspiration crop coefficients as a function of growing degree days, days after emergence, leaf area index, fractional green canopy cover, and plant phenology for soybean. Trans. ASABE 56, 1785–1803. https://doi.org/10.13031/trans.56.10219

Johnson, B., Thompson, C., Giri, A., NewKirk, S.V., 2011. Nebraska Irrigation Fact Sheet. Report No. 190. Department of Agricultural Economics, University of Nebraska–Lincoln.

Li, F.Q., Kustas, W.P., Prueger, J.H., Neale, C.M.U., Jackson, T.J., 2005. Utility of remote sensing-based two-source energy balance model under low- and high-vegetation cover conditions. J. Hydrometeorol. 6 (6), 878–891. https://doi.org/10.1175/jhm464.1

Lo, T., Heeren, D.M., Martin, D.L., Mateos, L., 2016. Pumpage reduction by using variable rate irrigation to mine undepleted soil water. Trans. ASABE 59, 1285–1298. https://doi.org/10.13031/trans.59.11773

Maguire, M., 2018. An Evaluation of Unmanned Aerial System Multispectral and Thermal Infrared Data as Information for Agricultural Crop and Irrigation Management. M.S. Thesis. Department of Biological Systems Engineering, University of Nebraska–Lincoln, Lincoln, Nebr. http://digitalcommons.unl.edu/biosysengdiss/82

Mendes, W.R., Araujo, F.M.U., Dutta, R., Heeren, D.M., 2019. Fuzzy control system for variable rate irrigation using remote sensing. Expert Syst. Appl. 124, 13–24. https://doi.org/10.1016/j.eswa.2019.01.043

Miller, K.A., Luck, J.D., Heeren, D.M., Lo, T., Martin, D.L., Barker, J.B., 2017. A geospatial variable rate irrigation control scenario evaluation methodology based on mining root zone available water capacity. Precis. Agric. 19, 666. https://doi.org/10.1007/s11119-017-9548-z

Neale, C.M.U., Bausch, W.C., Heerman, D.F., 1989. Development of reflectance-based crop coefficients for corn. Trans. ASAE 32, 1891–1899.

Neale, C.M.U., Geli, H.M.E., Kustas, W.P., Alfieri, J.G., Gowda, P.H., Evett, S.R., Prueger, J.H., Hipps, L.E., Dulaney, W.P., Chavez, J.L., French, A.N., Howell, T.A., 2012. Soil water content estimation using a remote sensing based hybrid evapotranspiration modeling approach. Adv. Water Resour. 50, 152–161. https://doi.org/10.1016/j.advwatres.2012.10.008

Norman, J.M., Kustas, W.P., Humes, K.S., 1995. Source approach for estimating soil and vegetation energy fluxes in observations of directional radiometric surface temperature. Agric. For. Meteorol. 77, 263–293. https://doi.org/10.1016/0168-1923(95)02265-Y

O'Shaughnessy, S.A., Evett, S.R., Andrade, M.A., Workneh, F., Price, J.A., Rush, C.M., 2016. Site-specific variable-rate irrigation as a means to enhance water use efficiency. Trans. ASABE 59, 239–249. https://doi.org/10.13031/trans.59.11165

O'Shaughnessy, S.A., Evett, S.R., Colaizzi, P.D., Andrade, M.A., Marek, T.H., Heeren, D.M., Lamm, F.R., LaRue, J.L., 2019. Identifying advantages and disadvantages of variable rate irrigation – An updated review. Appl. Eng. Agric. 35(6): 837-852. https://doi.org/10.13031/aea.13128

Raes, D., Steduto, P., Hsiao, T.C., Fereres, E., 2017. "Chapter 3: Calculation Procedures." AquaCrop Version 6.0 Reference Manual. March 2017. Food and Agriculture Organization of the United Nations, Rome, Italy.

Ramirez-Cuesta, J.M., Kilic, A., Allen, R., Santos, C., Lorite, I.J., 2017. Evaluating the impact of adjusting surface temperature derived from Landsat 7 ETM+ in crop evapotranspiration assessment using high-resolution airborne data. Int. J. Remote Sens. 38 (14), 4177–4205.

Ramirez-Cuesta, J.M., Allen, R.G., Zarco-Tejada, P.J., Kilic, A., Santos, C., Lorite, I.J., 2019. Impact of the spatial resolution on the energy balance components on an open-canopy olive orchard. Int. J. Appl. Earth Obs. Geoinf. 74, 88–102. https://doi.org/10.1016/j.jag.2018.09.001

Rondeaux, G., Steven, M., Baret, F., 1996. Optimization of soil-adjusted vegetation indices. Remote Sens. Environ. 55 (2), 95–107. https://doi.org/10.1016/0034-4257(95)00186-7

SCS, 1985. Part 630 Hydrology National Engineering Handbook Chapter 10 Estimation of Direct Runoff From Storm Rainfall.

Schaible, G., Aillery, M., 2015. Irrigation and Water Use. Accessed on 20 October 2018. http://www.ers.usda.gov/topics/farm-practices-management/irrigation-water-use.aspx

Shelton, D.P., Jasa, P.J., 2009. Estimating percent residue cover using the line-transect method. NebGuide G-1931. University of Nebraska–Lincoln Extension. https://digitalcommons.unl.edu/biosysengfacpub/632

Shulski, M.D., Cooper, S., Roebke, G., Dutcher, A., 2018. The Nebraska Mesonet: technical overview of an automated state weather network. J. Ocean. Atmosph. Technol. 35 (11), 2189–2200.

Stone, K.C., Bauer, P.J., Busscher, W.J., Millen, J.A., Evans, D.E., Strickland, E.E., 2015. Variable-rate irrigation management using an expert system in the eastern coastal plain. Irrig. Sci. 33, 167–175. https://doi.org/10.1007/s00271-014-0457-x

Stone, K.C., Sadler, E.J., 2016. Assessing spatial variation of corn response to irrigation using a Bayesian semiparametric model. Trans. ASABE 59, 251–261. https://doi.org/10.13031/trans.59.10942

Sui, R., Yan, H., 2017. Field study of variable rate irrigation management in humid climates. Irrig. Drain. 66, 327–339. https://doi.org/10.1002/ird.2111

U.S.G.S, 2018. Landsat 7 (L7) Data Users Handbook Version 1.0. Dep. Inter. U.S. Geol. Surv. 1. pp. 142.

U.S.G.S, 2019. Landsat 8 (L8) Data Users Handbook Version 4.0. Dep. Inter. U.S. Geol. Surv. 4, pp. 106.

Woldt, W.E., Neale, C.M.U., Heeren, D.M., Frew, E., Meyer, G.E., 2018. Improving agricultural water efficiency with unmanned aircraft. In: Association for Unmanned

Vehicle Systems International (AUVSI) XPONENTIAL Trade Show and Conference. Denver, Colo. 8 pages.

Vanella, D., Ramirez-Cuesta, J.M., Intrigliolo, D.S., Consoli, S., 2019. Combining electrical resistivity tomography and satellite images for improving evapotranspiration estimates of Citrus orchards. Remote Sens. 11, 373.

Yonts, C.D., Melvin, S.R., Eisenhower, D.E., 2008. Predicting the last irrigation of the season. NebGuide G1871.